The Dual-Mode Dipole: A New Array Element for 7T Body Imaging with Reduced SAR

Georgiy Solomakha, Carel van Leeuwen, Alexander Raaijmakers, Constantin Simovski, Alexander Popugaev, Redha Abdeddaim, Irina Melchakova, Stanislav Glybovski

The Dual-Mode Dipole: A New Array Element for 7T Body Imaging with Reduced SAR

Georgiy Solomakha[1,*], Carel van Leeuwen[2], Alexander Raaijmakers[2,6], Constantin Simovski[3], Alexander Popugaev[4], Redha Abdeddaim[5], Irina Melchakova[1], Stanislav Glybovski[1],

1 Department of Nanophotonics and Metamaterials, ITMO University, Saint Petersburg, Russian Federation

2 Department of Radiology, University Medical Center Utrecht, Utrecht, The Netherlands

3 Department of Electronics and Nanoengineering, Aalto University, School of Electrical Engineering, Espoo, Finland

4 RF and SatCom Systems, Fraunhofer Institute for Integrated Circuits IIS, Erlangen, Germany

5 Aix Marseille University, CNRS, Centrale Marseille, Institut Fresnel, Marseille, France

6 Department of Biomedical Engineering, Eindhoven University of Technology, Eindhoven, The Netherlands

***** Corresponding author:

Name Georgiy Solomakha
Department Department of Nanophotonics and Metamaterials
Institute ITMO University
Address 49 Kronverksky Pr.
197101
Russian Federation
E-mail g.solomakha@metalab.ifmo.ru

Running Head: Dual-mode dipole with low SAR

Manuscript words: 5389

Abstract

Purpose: To design and test an RF-coil based on two orthogonal eigenmodes in a pair of coupled dipoles, for 7 Tesla body imaging with improved SAR, called *dual-mode dipole*.

Methods: The proposed coil consists of two dipoles and creates two orthogonal field distributions in a sample (the even and odd modes). A coupler used to excite the modes was miniaturized with the conductor track routing technique. Numerical simulations of the dual-mode dipole in the presence of a homogeneous phantom were performed. Moreover, an array of such coils was simulated with a voxel body model. For comparison, a fractionated dipole combined with a surface loop coil was also simulated. Both coils were tested in a 7 Tesla MRI system on a phantom. Subsequently four dual-mode dipoles or dipole/loop combinations were used for a comparison of imaging performance in a human volunteer.

Results: Using the even mode of the dual-mode dipole showed 70% SAR reduction in comparison to the fractionated dipole while having the same B_1^+ in the prostate region. The odd mode of the dual-mode dipole showed a performance comparable to the surface loop both for SAR and B_1 efficiency. The obtained results showed that the proposed coil while creating lower SAR gave images of the same quality as the reference coil.

Conclusions: It was demonstrated that the array of dual-mode dipoles provided the same SNR and prostate imaging quality as the reference array, while demonstrating lower SAR. This is due to a smoother current distribution over a sample surface.

Keywords: Dipole, coil, modes, parallel transmit, SAR

INTRODUCTION

Imaging of a human body at ultrahigh fields (UHF) (7 Tesla (T) and higher) is difficult due to wave effects such as interference caused by the reduced wavelength in body tissues. This is because the region of interest (ROI) dimensions become comparable to the wavelength [1]. Moreover, an electromagnetic wave propagating through tissues at higher Larmor frequencies decays faster than at frequencies of clinical systems (1.5 and 3 T). Both effects deteriorate the B_1 field homogeneity and reduce the transmit efficiency of radiofrequency (RF) coils, thereby causing scarcely avoidable image artifacts. To increase the transmit efficiency and homogenize the B_1 pattern in the ROI, the parallel transmit (pTx) approach is widely used [2–4]. This approach allows for the manipulation of the transmit field distribution by the use of individual channels with customized phases and/or magnitudes of signals that drive a phased array surrounding the subject. The so-called RF-shimming procedure, allows for optimization of the transmit field with respect to various properties, such as: transmit homogeneity in the ROI, maximum transmit field per unit power [5] or reduced specific absorption rate (SAR) [6]. The power delivered to the pTx array is restricted by a limit to the maximum local SAR [7]. Therefore, the local SAR distribution needs to be evaluated. This is usually done at the RF-design stage using numerical simulations with detailed human models [8]. The same array as used for parallel transmission [9] or a separate one [10] can be used for parallel reception. Many useful RF coil designs have been demonstrated as elements of transmit arrays for body imaging at 7 T, including surface loops [11], dipoles [12–14], TEM-coils [15] and traveling-wave antennas [16].

Dipole antennas have been recently shown to be the most efficient in deeply located ROIs in a human body at 7 T, e.g. in prostate imaging applications [17]. The choice of dipole elements for reception as well could be explained by the fact that linear currents flowing along the direction of B_0 are preferable when reaching the ultimate signal-to-noise ratio (SNR) in a cylindrical subject, which is a rough approximation of a human torso [18]. In order to realize linear currents with a desirable distribution, multiple designs of dipoles have been proposed. The length and current distribution of a dipole are responsible for both transmission and reception properties and can be controlled using several approaches. Among them are lumped reactive circuit elements [13], loading by high-permittivity dielectric slabs [19] and shaping conductors of a dipole (i.e. meandering or branching) [17]. One recent design is the fractioned dipole antenna; a straight printed dipole with several structural inductances included in its branches [13]. This design provides the lowest maximum

local SAR for the same amount of B_1^+ in the ROI among existing dipoles in the prostate imaging application [13].

To further improve the performance of a transceive array coil for body imaging at 7 T, the number of independent channels can be increased. More channels provide more degrees of freedom in transmission (i.e. in the RF-shimming procedure) and increase the SNR in reception. However, increasing the number of elements in dipole arrays is intrinsically limited by inter-element coupling, which leads to difficulties in tuning and matching of individual array elements and unacceptably high scattering power losses. To avoid mutual coupling between two dipoles, several resonant decoupling techniques can be used [20–23]. However, no resonant decoupling techniques applicable to multi-element dipole arrays for body imaging with arbitrary shimming phases have been demonstrated so far. In this situation, the only way to increase the number of array channels and avoid any further reduction in inter-element distance, is to use modified multi-mode elements instead of single-mode dipoles. By overlapping a dipole with another antenna in each element position, thus producing an orthogonal distribution of currents and RF-fields not affecting the dipole, the number of elements can be doubled. This idea has recently been implemented as a new dual-mode element of a 7 T transceive array where each dipole was combined with a surface loop. As a result, adding the loop elements decreased SAR and improved the B_1^+ magnitude at a fixed total accepted power [24].

A single dipole is a resonant antenna with a linear current distribution creating RF-fields mostly described by an electric dipole moment directed in parallel to the subject's surface. In contrast, a surface loop antenna produces the field in the subject similarly to a magnetic dipole, directed normally to the surface. This is, however, not the only one known combination of antennas that may be placed in the same position avoiding mutual coupling due to the orthogonality of created RF-fields. In theoretical works, it has been shown that mutually orthogonal and resonant electric and magnetic dipole moments can be simultaneously excited also in parallel cut-wires [25–29]. A pair of straight metal wire antennas may possess an even mode with parallel currents (also called electric dipole mode) and an odd mode with anti-parallel currents (also called electric quadrupole mode). The odd mode at electrically short distances, produces a magnetic field similar to a continuous loop located in the same plane. This agrees with the fact that an off-diagonal electric quadrupole produces the same near-field distribution as a magnetic dipole [30]. The even mode produces RF fields similarly to a single straight wire dipole, but only at sufficient distances from the wires. Importantly, this similarity schematically shown in Fig. 1 does not hold in the case of close proximity to the wires.

In this work we propose and test a new dual-mode array element for body imaging at 7 T composed of two identical coupled dipoles called the *dual-mode dipole*. By independent excitation of the even and odd modes of the dipole pair, two different field distributions can be created in the prostate region (ROI) which are very similar to the ones created by the aforementioned dipole-loop antenna [24]. The latter is taken as a *reference coil* for numerical and experimental comparison. The aim of this work is to demonstrate that the dual-mode dipole reaches the same transmit efficiency as the reference coil but has reduced SAR due to a more homogeneous current distribution over the subject's surface.

METHODS

Proposed coil design

The dual-mode dipole is composed of two identical fractionated dipole antennas of the length $l_{\mathrm{D}} = 300$ mm placed parallel to each other at distance s as shown in Fig. 2 (a). The dipoles of the proposed coil have two symmetric ports in their middle splits. The even mode can be excited when the ports are driven in-phase, while the odd mode is excited by the out-of-phase drive. Due to the orthogonality of these two modes they could be excited independently. This dual-mode excitation can be realized by using an appropriate 180° hybrid. The latter is a device used for coupling/dividing RF-signals with equal amplitudes but with same or opposite phases depending on a driven input. It is very similar to a quadrature hybrid commonly used to drive the CP mode of a bird-cage coil [31]. The difference is in the introduced phase delay (180° in our case instead of 90°). A conventional rat-race coupler has four ports, separated by three $\lambda/4$ delay lines and one $3\lambda/4$ line forming a ring as shown in Fig. 2 (b). The ring should have a characteristic impedance $\sqrt{2}Z_0$, where Z_0 is the impedance of ports (in MRI systems Z_0 is commonly equal to 50 Ω). An RF-signal applied to the even input port is split between outputs 1 and 2 with equal phases, while the odd port is isolated. In case, the odd input port is fed, the signal is split between the same outputs out of phase, while the even port is isolated. In our case, these properties of the coupler allow independent excitation of the even and odd modes of the two dipoles. Thus the outputs of the coupler should be connected to the ports of the dipoles. To minimize losses in the delay lines the coupler together with the dipoles was printed on the same dual-layer PCB with Rogers 4003 substrate (ε=3.38, $\tan\delta$=0.002, thickness $h = 0.8$ mm).

Since a conventional coupler shown on the left side of Fig.2 (b) would occupy a relatively

large area ($2\pi \times 130 \times 130$ mm^2), a special conductor track routing technique [32] was applied to synthesize a more compact layout. The main idea of this miniaturization is to replace delay lines of the corresponding ring sections by densely packed meandered lines of the same characteristic impedance and electrical lengths. The lines were meandered as periodically repeated circular bends with outer radius $r_0 = 2.2$ mm as depicted on the right side of Fig. 2 (b). Since the input impedance of the dipoles amounts to approximately $Z_{\text{in}} \approx 70\ \Omega$, the coupler was designed to have the input and output impedance of $Z_0 = 71\ \Omega \approx Z_{\text{in}}$. To avoid placing extra baluns at the dipoles inputs, symmetric stripline topology was chosen for the coupler layout. The employed symmetric stripline used for the coupler was composed of two metal strips of the same width w symmetrically printed on the opposite sides of the substrate (see inset in Fig. 2 (b)). For the given substrate properties, the chosen value of w was 0.9 mm to reach the characteristic impedance of $\sqrt{2}Z_0 = 100\ \Omega$. It is worth noting that the symmetric layout had no ground plane. The overall coupler area was 40×70 mm^2, i.e. only 3 % of that of the conventional ring-shaped design. The coupler loaded by the dipoles at its outputs was matched to 50 Ω at both inputs by means of lumped elements. Ceramic baluns were employed at both the even-mode and odd-mode ports where coax cables were soldered to the board. The top PCB layer of a manufactured dual-mode dipole is shown on the photograph in Fig. 2 (c). Note that only one half of each dipole can be seen on the photograph as the opposite one was printed on the bottom layer.

The reference coil consisted of a fractionated dipole and a surface rectangular loop of the sizes $b \times l_{\text{L}} = 89 \times 190$ mm^2. The dipole and loop were printed on separate 1-mm-thick FR-4 substrates and then overlapped (ε=4.4, $\tan\delta$=0.02) as shown in Fig. 2 (d). Four lumped capacitors were distributed around the loop for tuning to the Larmor frequency.

Simulation

Numerical simulation software CST Studio Suite (CST, Darmstadt, Germany) was used to choose the separation s between two dipoles in the dual-mode dipole by parametric optimization. Also, it was used to calculate the electromagnetic fields produced by the proposed and the reference coils in pelvis-shaped homogeneous phantom with electrical properties ε=61.8, ς=0.87 S/m. The corresponding numerical models are shown in Fig. 3 (a,b). Each model contained approximately $2.5 \cdot 10^5$ mesh cells. Adaptive meshing was performed at 297.2 MHz using Frequency Domain Solver.

For evaluation of local SAR and B_1^+ distributions in a voxel model of a human body the Time Domain Solver was used with the commercially available models (Gustav, CST Virtual Family and

Tom, CST VHP). The models of four-element arrays composed of dual-mode dipoles and reference coils are shown in Fig. 3 (c,d). Each model had approximately $2 \cdot 10^7$ mesh cells. Local mesh on the surface of the coils was applied to improve the accuracy of the calculation. This simulation also gave S-parameters of the array elements of both types. In each case two of four dual-mode coils were positioned on top of a subject and the other two were placed at the bottom. In the proposed coil two branches of each of the dipoles were printed on the opposite sides of the same substrate as can be seen in Fig. 2 (a,c). However, in the simulations, we put the dipoles completely on one side of the PCB for simplicity as shown in Fig. 3 (b,d).

Calculated field distributions were normalized to the square root of the accepted power P_{acc} to determine the transmit efficiency. Phase shimming for both the compared arrays was performed by optimizing for the maximum $B_1^+/\sqrt{P_{\text{acc}}}$ in the prostate region of the voxel model. Here, a fixed applied power was provided for each of eight channels (equal RF-signal magnitudes). At the same time the required optimal phases were determined for in-phase summation of magnetic fields of individual channels in the prostate.

Both coils were tuned to 297.2 MHz, the proton Larmor frequency at 7 T, and matched to 50 Ω with S_{11} better than -15 dB for each channel. The rat-race coupler for modes excitation and lumped element matching circuits were taken into account in schematic co-simulation with the CST Design Studio module. To match port impedances of the reference coil, LC-circuits with the pi-shaped topology were used in each case. The series inductance was realized as a self-made wire winding, while the parallel capacity was implemented using commercially available non-magnetic capacitors. For the dual-mode dipole, the same matching approach was used with series capacitors instead of series inductors.

To evaluate the performance of the designed miniaturized rat-race coupler the latter was also simulated using frequency domain solver of CST. The local mesh was assigned onto the surfaces of conductors to ensure high convergence accuracy. The numerical model consisted of approximately $2.5 \cdot 10^5$ mesh cells. Adaptive meshing was performed at the Larmor frequency.

Measurements and performance evaluation

To evaluate the performance of the dual-mode dipole as an array element, four identical coils were manufactured (see Fig. 2 (c)). For the experimental comparison, four reference coils were also manufactured (see Fig. 2 (d)). All the array elements were matched to 50 Ω with the measured reflection coefficients at both input ports better than -10 dB when loaded by a homogeneous phan-

tom. The measured transmission coefficient between the two ports was better than -15 dB for both the proposed and the reference coils.

Measurements were performed on a 7T Philips Achieva platform (Philips Healthcare, Best, The Netherlands). First, a homogeneous phantom was used to measure B_1^+ patterns created by the dual-mode dipole and the reference coil as single elements located symmetrically on the top of the phantom. The dual-TR method [33] was used with a 3D gradient echo sequence to obtain B_1 maps, using the following parameters: TE/TR1/TR2: 2.172/50/250 ms, $1.25 \times 1.25 \times 10$ mm^3, FA=60°. Power measured at coil plugs of the proposed coil was equal to 29.62 W both for the even and odd channels. For the reference coil, the measured input power was equal to 30.64 W both for the dipole and loop channels.

T2-weighted *in-vivo* body images (TR/TE=2500/90 ms, 0.5×0.5×4 3 mm^3, TSE-factor 9) were obtained using the manufactured arrays. SNR maps were acquired as well. The SNR values were determined according to the method described in [34].

The study was approved by the local medical ethics committee and informed consent was obtained from each subject.

RESULTS

Simulation

Simulated S-parameters of the miniaturized rat-race coupler in the frequency range from 280 to 320 MHz are presented in Fig. 4. From the plots, one can see that the coupler performs very close to an ideal 180° coupler. Namely, the transmission from both the input ports to each of the output ports is very close to -3 dB (the insertion losses do not exceed 0.4 dB). At the central operational frequency of 300 MHz the phase difference between the output signals is almost equal to 0° or 180° depending on the driven input port (within 1°-accuracy). The reflection coefficient at both the inputs is lower than -17 dB, while the isolation between the odd and even inputs is better than -35 dB.

The calculated B_1^+ distributions in the central transversal plane of the phantom normalized by the square root of the accepted power $\sqrt{P_{\text{acc}}}$ is presented in Fig. 5. The results are presented for two orthogonal channels of the dual-mode dipole (a,b) and the reference coil (c,d). The colour plots demonstrate the B_1^+ magnitude distribution in the phantom, while the vector plots show the moment directions of the magnetic field vector. These plots demonstrate that B_1^+ distributions of

the proposed coil are very similar to the ones of the reference coil at the depth of the phantom. As can be seen in Fig. 5 (a) the vertical magnetic field component is dominating in the odd-mode pattern of the proposed coil, while the magnitude pattern is quite asymmetric. In fact, the loop coil produces a similar field pattern (see Fig. 5 (c)). The calculated magnetic field patterns of the dual-mode dipole's even mode are shown in Fig. 5 (b). The latter exhibits the dominant horizontal magnetic field component and a reasonably symmetric B_1^+ pattern. This pattern looks similar to one created by the fractionated dipole [13] in the middle region of the phantom (see Fig. 5 (d) for comparison). A channel-by-channel comparison of $B_1^+/\sqrt{P_{\text{acc}}}$ vs. the depth profiles of the dual-mode dipole and the reference coil is given in Fig. 6 (a,b). The profiles correspond in each case to the depth coordinate lines marked in Fig. 5 with the red vertical dashed lines going through the magnitude maxima at the depth of 100 mm.

Insets in Fig. 5(a-d) present the calculated local SAR distributions for 1W of accepted power in the top coronal plane of the phantom. The maximum values of the SAR per unit accepted power are almost the same for the odd mode of the proposed coil (5 (a)) and the loop (5 (c)). In contrast, the even mode of the proposed coil (5 (b)) creates much lower SAR than the single dipole does (5 (d)). To be specific for the same accepted power of 1 W, one obtains 1.03 W/kg with the even mode excitation instead of 2.41 W/kg provided by the single dipole. The lower maximum local SAR of the even mode goes along with the more uniform pattern of B_1^+ in the transverse plane in a close proximity of the phantom's surface in comparison to the dipole (compare insets of Fig. 5 (b) and (d)). The B_1^+ vs. depth profile curves for the dual-mode dipole and the reference coils, normalized to $\sqrt{\text{SAR}_{max}}$ are presented in Fig. 6 (c,d).

Fig. 7 presents numerical results for the eight-channel array configurations with dual-mode dipoles (first row) and reference coils (second row). The results correspond to the simulation geometries shown in Fig. 3 (c,d), which included Gustav voxel model. To obtain the maximum field magnitude in the prostate (indicated by the black contour in Fig. 7), phase-shimming was applied. Appropriate excitation phases were calculated for all eight channels, while the equal signal magnitudes were used. The magnetic field patterns normalized to the maximum 10-g averaged SAR ($B_1^+/\sqrt{\text{SAR}_{10g}}$) are depicted in Fig. 7 (a,d). The B_1^+ patterns normalized by the square root of the total power accepted by the array ($B_1^+/\sqrt{P_{\text{acc}}}$) are given in Fig. 7 (b,e). The distributions of SAR_{10g} for the same total accepted power of 1W are given in Fig. 7 (c,f).

The full numerically calculated eight-port scattering matrix is presented in Fig. 8 (a) for the array of dual-mode dipole and in Fig. 8 (b) for the reference array. Indices of S-parameters

correspond to the port numbers indicated in Fig. 7. Odd numbers correspond to odd mode ports of the proposed coils and to loop ports of the reference coils. Even numbers correspond to even mode ports of the proposed coils and to dipole ports of the reference coils.

To predict the sensitivity of both arrays to the variation of the load, an additional simulation was performed with Tom voxel model having a different BMI. For this purpose the bottom element with the ports No. 7 and 8 was considered. As can be seen from Fig. 7 (c,f) this element is located most closely to the maximum local SAR region. The other array elements were found to have weaker variation of return loss with respect to the load. The return losses of the selected element (i.e. S_{77} and S_{88} magnitudes) were compared channel-by-channel for the two arrays in the presence on both body models in Fig. 8 (c,d).

Measurements

Measured B_1^+ field distributions in the central transverse plane, obtained by using a single dual-mode dipole on top of the phantom, are shown for the odd (a) and the even (b) channels in Fig. 9. For comparison, the measured B_1^+ created by the loop and the dipole of the reference coil are shown in Fig. 9 (c) and (d) correspondingly. The penetration profiles of the measured B_1^+ per unit accepted power were calculated from the measured maps along the depth coordinate axes represented by the red dashed lines in Fig. 9 (a,b,c,d). The resulting profiles are shown in Fig. 9(e,f). The body images and SNR maps in the central transverse plane of the prostate of a healthy volunteer obtained using the four-element array of the proposed dual-mode coils are presented in the first row of Fig. 10. For comparison, similar images and SNR maps obtained using the reference array are presented in the second row.

DISCUSSION

The proposed idea of assembling an element of a parallel-transmit array for 7 T body imaging of two closely-spaced and coupled dipoles has been carefully studied in this work both numerically and experimentally. By numerical simulations, we compared the field distributions created by the dual-mode dipole to ones of a single fractionated dipole and a surface loop.

The design of the new coil uses two identical fractionated dipoles exactly like the dipole from the reference coil. The even and odd modes of the dual-mode dipole are excited using a novel miniaturized rat-race coupler integrated into the coil. To determine the separation s between them,

a parametric numerical optimization was made with the aim to fit the same transmit efficiency as that of the reference coil's channels in the ROI (i.e. in the prostate region). As a result, the even mode of the proposed coil reached the same B_1^+ for a given power in the middle of the phantom (at the depths of 6-10 cm) as compared to the fractionated dipole. The same equivalence of the transmitted field was observed for the odd mode of the proposed coil and the reference loop. This equivalence only took place with the optimal value $s = 60$ mm. For smaller s the odd mode was less efficient than the loop, while the even mode was more efficient than the dipole. The opposite imbalance was observed for s larger than the optimum. Moreover, from Fig. 5 and Fig. 6(a,b) it is clearly seen that the B_1^+ distributions produced by the even and odd modes of the dual-mode dipole for a given accepted power in the phantom are qualitatively and quantitatively similar to ones of the dipole and loop (respectively) at depths larger than 6 cm. Noticeably, the dipole created higher and less uniform B_1^+ per unit accepted power on the surface of the phantom than the proposed coil at its even mode. At the same time, the even mode resulted in 2.41 times lower maximum local SAR on the phantom surface, as can be seen comparing the insets of Fig. 5 (b) and (d). This improvement of SAR can be explained by a more homogeneous distribution of electric currents at the surface of a sample.

As demonstrated by simulations with a voxel body model, SAR performance of the dual-mode dipole as an eight-element array element is still better than the dipole-loop combination. Indeed, when the B_1^+ per unit total accepted power is maximized in the prostate region by phase shimming, the maximum 10-g averaged SAR for the same power is 58 % lower. At the same time B_1^+ in the prostate was almost the same for the two compared arrays (see Fig. 7).

From the calculated S-parameters of the arrays presented in Fig. 8 (a,b), it follows that the coupling between even-mode channels of two adjacent proposed coils is higher than for two single dipoles. However, the transmission coefficient between the corresponding ports of the array elements in both cases holds lower than -17 dB, which is acceptable. Therefore, for the dipole mode, splitting the current into two in-phase and parallel currents improves the maximum local SAR but does not significantly affect the inter-element coupling.

Measured B_1^+ per unit accepted power patterns are in good agreement with the simulations results (compare Fig.5 and Fig. 9(a-d)). Indeed, it was experimentally confirmed that the corresponding channels of the dual-mode dipole and the reference coil are equivalent except for the top surface of the phantom. In this region, the even mode of the proposed coil created more distributed magnetic field. Together with the SAR simulation results this agreement indirectly supports the

conclusion of lower maximum local SAR provided by our dual-mode dipoles.

The *in-vivo* results (i.e. prostate images and SNR maps shown in Fig. 10) demonstrate almost the same imaging performance provided by the arrays of dual-mode dipoles and reference coils. Thus in the prostate region the relative SNR was equal to 275 for the array of dual-mode dipoles versus 284 for the reference array. Moreover, the proposed array created no additional inhomogeneity artifacts in comparison to the reference array.

CONCLUSION

In this work we numerically and experimentally compared two dual-mode coils: the proposed one, consisting of two properly driven fractionated dipoles, and the reference one, consisting of a fractionated dipole and a surface loop. Both approaches double the total number of transceive array channels, which improves performance in body imaging at 7 Tesla.

It was clearly demonstrated that the proposed dual-mode dipole is equivalent to the dipole-loop combination in terms of B_1^+ per unit power in the prostate region. At the same time, a 58% reduction in the maximum whole-body local SAR is achieved using an eight-channel array of the proposed coils. The improved SAR performance of our coil is explained by the currents of its even mode. The latter are more homogeneously distributed over a subject causing lower electric fields for the same accepted power. Importantly, this advantage over the reference array of dipole-loop combinations has been observed in the simulations with two different voxel body models. Moreover, the modified current distributions of the even and odd modes of the proposed coil did not considerably increase the inter-element coupling in comparison to the reference array with the same element number.

To test the coil on a healthy volunteer, body images were obtained with four dipole pairs (eight independent channels), which demonstrated similar imaging capabilities in comparison to the reference array.

In conclusion, the proposed idea of splitting an electric current of each array element into two parallel paths relaxes SAR-related constraints for body imaging at ultrahigh fields. At the same time, the demonstrated dual-mode dipole provides almost the same imaging capabilities and inter-element coupling as a state-of-the-art array of combined dipole-loop coils.

ACKNOWLEDGMENTS

This work was supported by the Ministry of Education and Science of the Russian Federation (project No. 14.587.21.0041 with the unique identifier RFMEFI58717X0041) and European Union Horizon 2020 research and innovation programme under the grant agreement No. 736937. The authors are grateful to Mrs. Anna Hurshkainen of ITMO University, Department of Nanophotonics and Metamaterials, for her help and advice in numerical simulations of UHF coils, and Mr. Andrey Sayanskiy of ITMO University, Department of Nanophotonics and Metamaterials, for his help in post-processing of RF fields, Mr. Ingmar Voogt of UMC, Department of Radiology, Coil Laboratory, for his help and advice on UHF-body coil design and Mr. Bart Steensma of UMC, Department of Radiology, for his help and advice on SNR mapping and raw data post-processing.

References

1 Vaughan JT, Snyder CJ, DelaBarre LJ, Bolan PJ, Tian J, Bolinger L, et al. Whole-body imaging at 7T: Preliminary results. Magnetic Resonance in Medicine. 2009;61(1):244–248.

2 Brink W, Gulani V, Webb A. Clinical applications of dual-channel transmit MRI: A review. Journal of Magnetic Resonance Imaging. 2015 10;42(4):855–869.

3 Webb AG, Collins CM. Parallel transmit and receive technology in high-field magnetic resonance neuroimaging. International Journal of Imaging Systems and Technology. 2010;20(1):2–13.

4 Katscher U, Börnert P. Parallel RF transmission in MRI. NMR in Biomedicine. 2006;19(3):393–400.

5 Deniz CM, Brown R, Lattanzi R, Alon L, Sodickson DK, Zhu Y. Maximum efficiency radiofrequency shimming: Theory and initial application for hip imaging at 7 tesla. Magnetic Resonance in Medicine. 2013;69(5):1379–1388.

6 van den Bergen Bob, van den Berg Cornelis A T, J KDW, W LJJ. SAR and power implications of different RF shimming strategies in the pelvis for 7T MRI. Journal of Magnetic Resonance Imaging. 2009;30(1):194–202.

7 van Osch MJP, Webb AG. Safety of Ultra-High Field MRI: What are the Specific Risks? Current Radiology Reports. 2014 Jul;2(8):61.

8 Kozlov M, Turner R. Fast MRI coil analysis based on 3-D electromagnetic and RF circuit co-simulation. Journal of Magnetic Resonance. 2009;200(1):147 – 152.

9 Roemer PB, Edelstein WA, Hayes CE, Souza SP, Mueller OM. The NMR phased array. Magnetic Resonance in Medicine. 1990;16(2):192–225.

10 Barberi EA, Gati JS, Rutt BK, Menon RS. A transmit-only/receive-only (TORO) RF system for high-field MRI/MRS applications. Magnetic Resonance in Medicine. 2000;43(2):284–289.

11 Zhu Y. Parallel excitation with an array of transmit coils. Magnetic Resonance in Medicine. 2004;51(4):775–784.

12 Raaijmakers AJE, Ipek O, Klomp DWJ, Possanzini C, Harvey PR, Lagendijk JJW, et al. Design of a radiative surface coil array element at 7 T: The single-side adapted dipole antenna. Magnetic Resonance in Medicine. 2011;66(5):1488–1497.

13 Raaijmakers AJE, Italiaander M, Voogt IJ, Luijten PR, Hoogduin JM, Klomp DWJ, et al. The fractionated dipole antenna: A new antenna for body imaging at 7 Tesla. Magnetic Resonance in Medicine. 2016;75(3):1366–1374.

14 Oezerdem C, Winter L, Graessl A, Paul K, Els A, Weinberger O, et al. 16-channel bow tie antenna transceiver array for cardiac MR at 7.0 tesla. Magnetic Resonance in Medicine. 2016;75(6):2553–2565.

15 Wu B, Zhang X, Wang C, Li Y, Pang Y, Lu J, et al. Flexible transceiver array for ultrahigh field human MR imaging. Magnetic Resonance in Medicine. 2012;68(4):1332–1338.

16 Brunner DO, De Zanche N, Fröhlich J, Paska J, Pruessmann KP. Travelling-wave nuclear magnetic resonance. Nature. 2009 Feb;457:994 EP –.

17 Raaijmakers AJE, Luijten PR, van den Berg CAT. Dipole antennas for ultrahigh-field body imaging: a comparison with loop coils. NMR in Biomedicine. 2016;29(9):1122–1130. NBM-14-0331.R1.

18 Lattanzi R, Wiggins GC, Zhang B, Duan Q, Brown R, Sodickson DK. Approaching ultimate intrinsic signal-to-noise ratio with loop and dipole antennas. Magnetic Resonance in Medicine. 2017;p. 1789–1803.

19 Brink WM, Paska J, Dai J, van Gemert JHF, Chen G, Wiggins GC, et al. Dielectric enhanced dipoles for MRI 2014; Approaching the ideal current pattern. In: 2017 International Conference on Electromagnetics in Advanced Applications (ICEAA); 2017. p. 1220–1223.

20 Yan X, Zhang X, Wei L, Xue R. Magnetic wall decoupling method for monopole coil array in ultrahigh field MRI: a feasibility test. Quantitative Imaging in Medicine and Surgery. 2014;4(2).

21 Georget E, Luong M, Vignaud A, Giacomini E, Chazel E, Ferrand G, et al. Stacked magnetic resonators for MRI RF coils decoupling. Journal of Magnetic Resonance. 2017;275:11 – 18.

22 Hurshkainen AA, Derzhavskaya TA, Glybovski SB, Voogt IJ, Melchakova IV, van den Berg CAT, et al. Element decoupling of 7T dipole body arrays by EBG metasurface structures: Experimental verification. Journal of Magnetic Resonance. 2016;269(Supplement C):87 – 96.

23 Yan X, Zhang X, Xue R, Gore JC, Grissom WA. Optimizing the ICE decoupling element distance to improve monopole antenna arrays for 7 Tesla MRI. Magnetic Resonance Imaging. 2016;34(9):1264 – 1268.

24 Ertürk MA, Raaijmakers AJE, Adriany G, Uğurbil K, Metzger GJ. A 16-channel combined loop-dipole transceiver array for 7 Tesla body MRI. Magnetic Resonance in Medicine. 2017;77(2):884–894.

25 Podolskiy VA, Sarychev AK, Narimanov EE, Shalaev VM. Resonant light interaction with plasmonic nanowire systems. Journal of Optics A: Pure and Applied Optics. 2005 feb;7(2):S32–S37.

26 Lagarkov AN, Sarychev AK. Electromagnetic properties of composites containing elongated conducting inclusions. Phys Rev B. 1996 Mar;53:6318–6336.

27 Panina LV, Grigorenko AN, Makhnovskiy DP. Optomagnetic composite medium with conducting nanoelements. Phys Rev B. 2002 Oct;66:155411.

28 Jouvaud C, Abdeddaim R, Larrat B, de Rosny J. Volume coil based on hybridized resonators for magnetic resonance imaging. Applied Physics Letters. 2016;108(2):023503.

29 Slobozhanyuk AP, Poddubny AN, Raaijmakers AJE, van den Berg CAT, Kozachenko AV, Dubrovina IA, et al. Enhancement of Magnetic Resonance Imaging with Metasurfaces. Advanced Materials. 2016;28(9):1832–1838.

30 Raab RE, de Lange OL. Multipole Theory in Electromagnetism. Oxford Science Publications, Oxford, UK; 2005.

31 Glover GH, Hayes CE, Pelc NJ, Edelstein WA, Mueller OM, Hart HR, et al. Comparison of linear and circular polarization for magnetic resonance imaging. Journal of Magnetic Resonance (1969). 1985;64(2):255 – 270.

32 Popugaev AE, Wansch R. A novel miniaturization technique in microstrip feed network design. In: 2009 3rd European Conference on Antennas and Propagation; 2009. p. 2309–2313.

33 Yarnykh VL. Actual flip-angle imaging in the pulsed steady state: A method for rapid three-dimensional mapping of the transmitted radiofrequency field. Magnetic Resonance in Medicine. 2007;57(1):192–200.

34 Peter K, R ME. Image reconstruction in SNR units: A general method for SNR measurement†. Magnetic Resonance in Medicine. 2005;54(6):1439–1447.

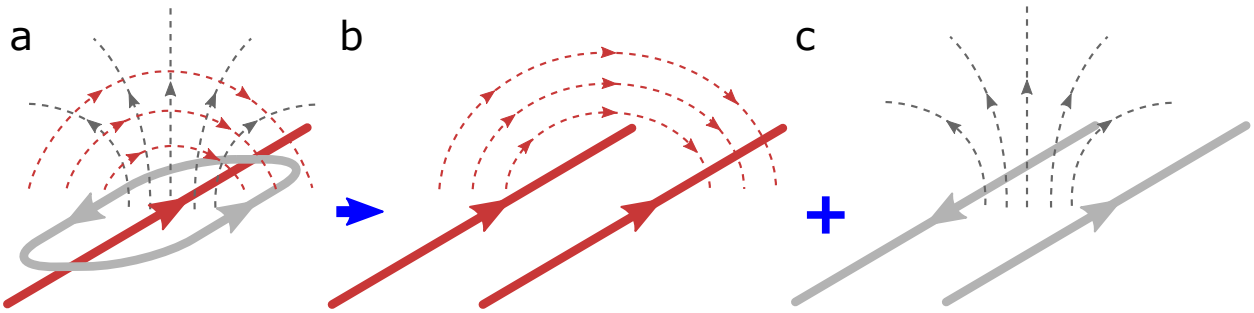

Figure 1: Analogy in magnetic fields created by combination of dipole and surface loop (a) and even mode (b) and odd mode (c) of two coupled dipoles.

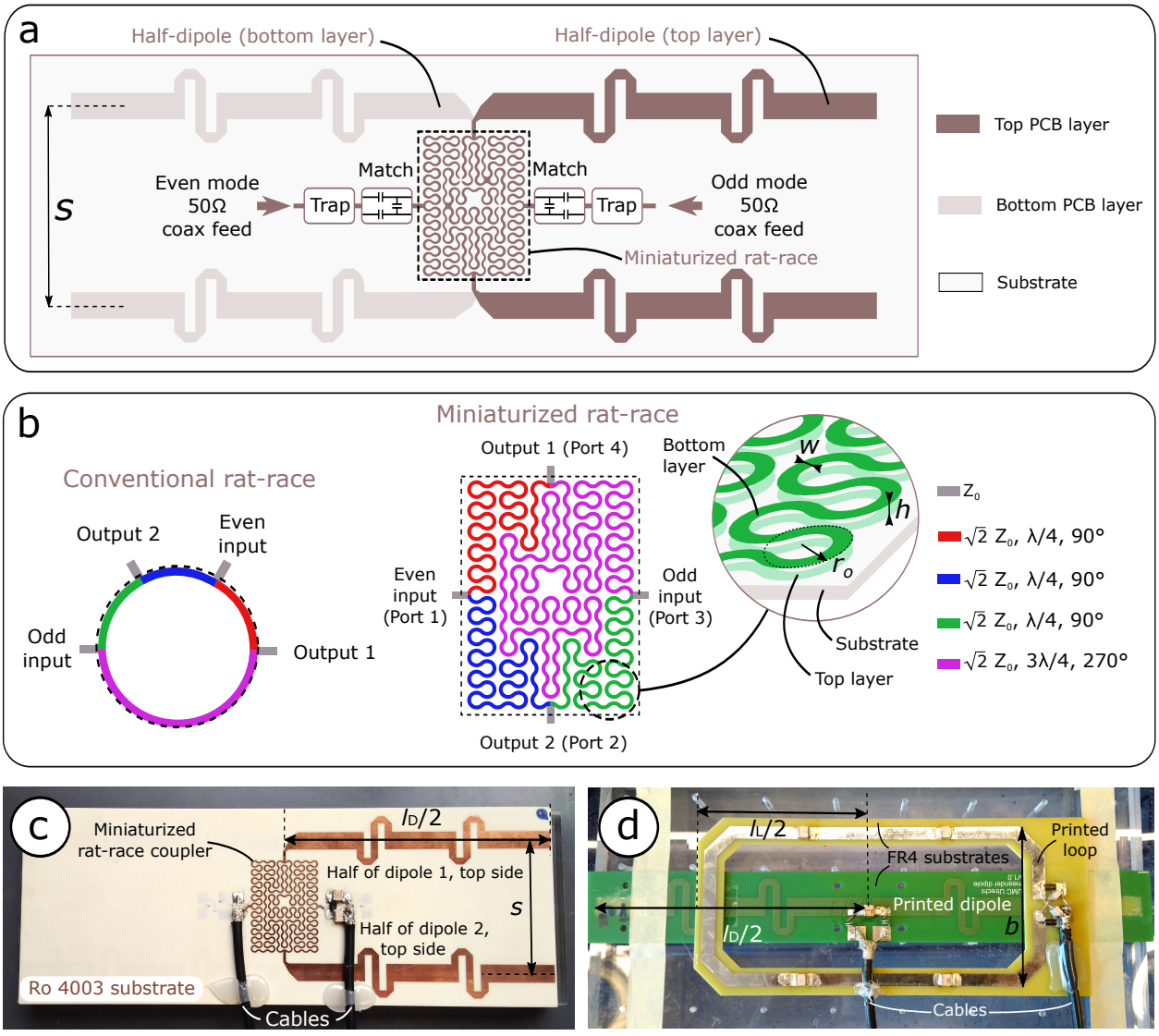

Figure 2: Proposed design of dual-mode dipole: (a) combined PCB layout with two fractionated dipoles and miniaturized rat-race coupler; (b) delay line interconnection of conventional ring rat-race coupler (left) and miniaturized rat-race coupler (right) (inset shows parameters of meandered symmetric strip-lines); (c) manufactured dual-mode dipole. Manufactured reference coil with dipole and loop (d).

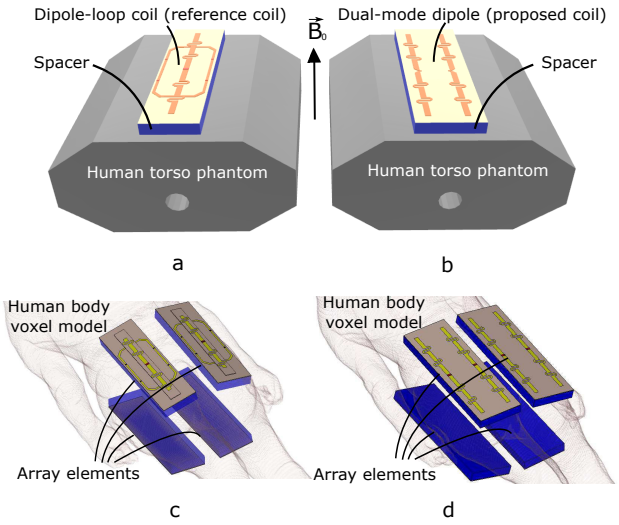

Figure 3: Simulation geometries: (a) single reference coil with homogeneous phantom; (b) single dual-mode dipole with the same phantom; (c) array of four reference coils with human body model; (d) array of four dual-mode dipoles with human body model.

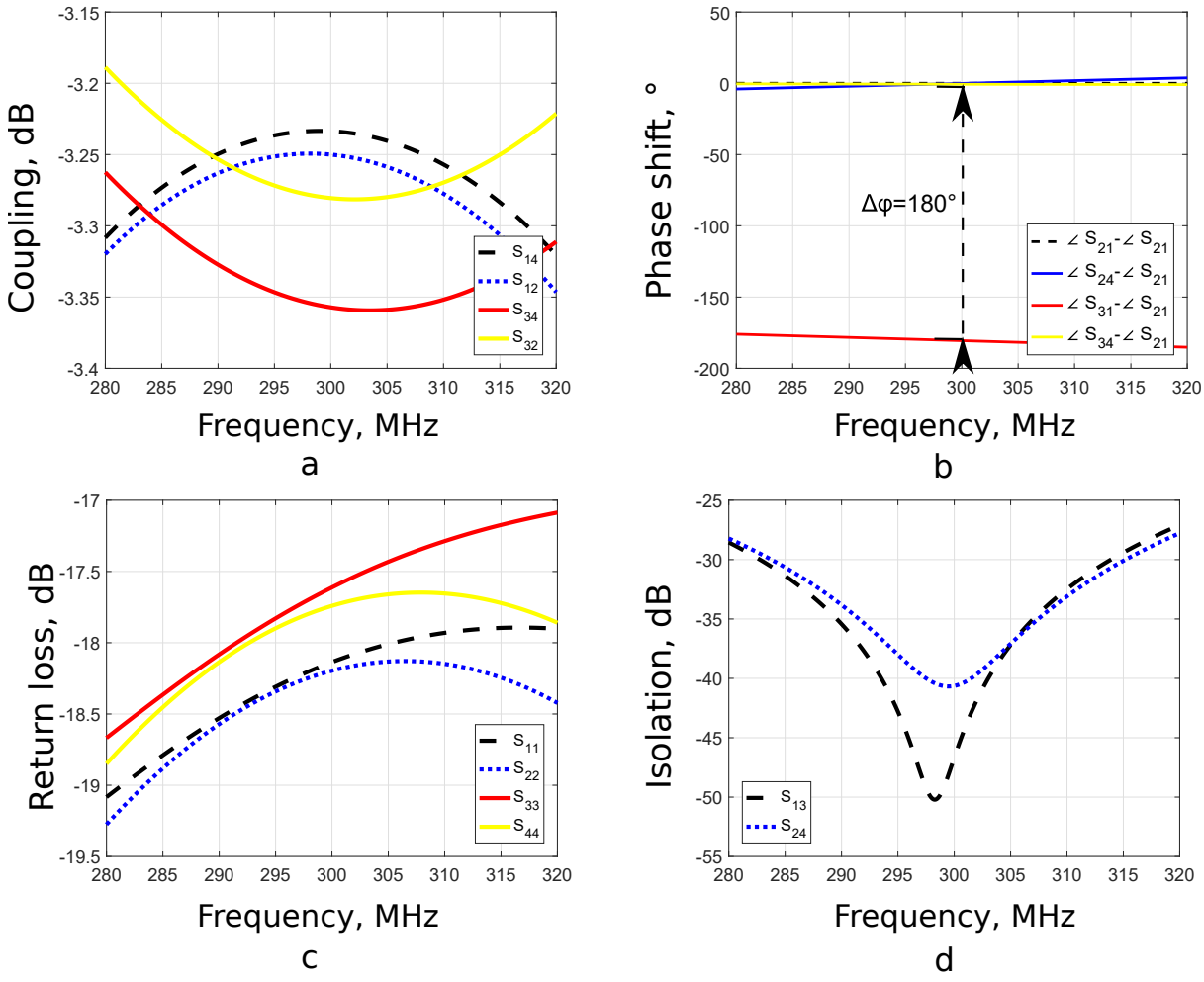

Figure 4: Simulated S-parameters of miniaturized rat-race coupler: (a) transmission coefficients from inputs to outputs; (b) phase delays from inputs to outputs (phase of S_{21} is taken as zero); (c) return losses (matching) of coupler inputs; (d) isolation between odd and even input ports S_{13} and between outputs 1 and 2 S_{24}.

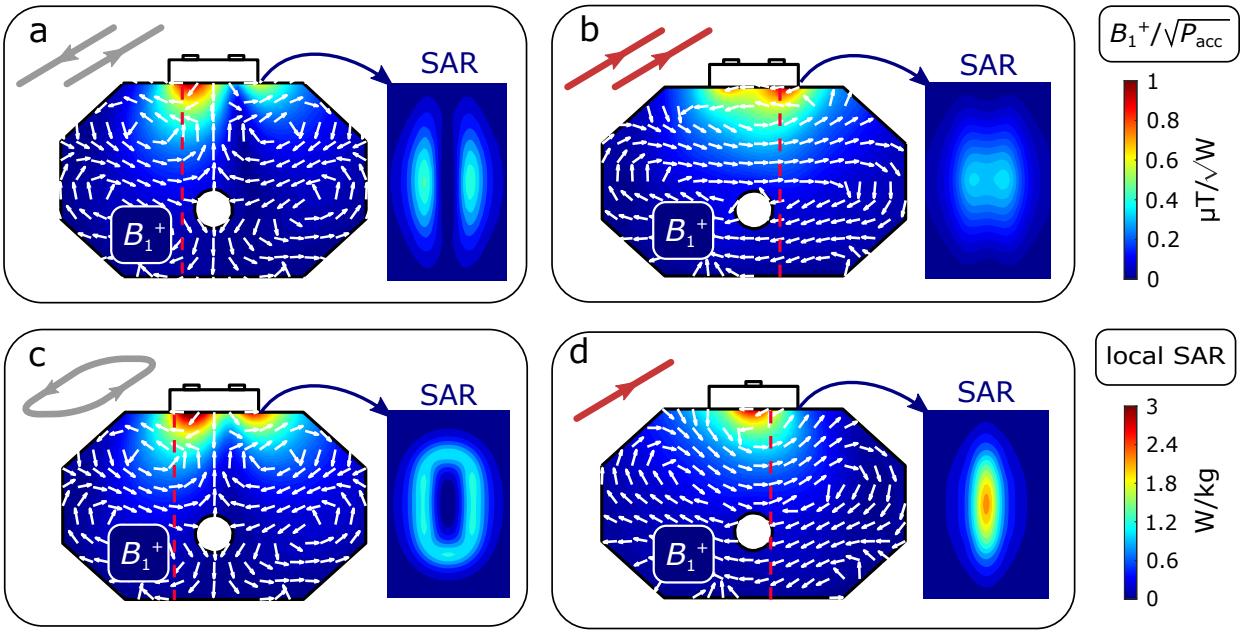

Figure 5: Simulated magnetic RF-field and local SAR distributions in phantom: (a) odd mode of dual-mode dipole; (b) even mode of dual-mode dipole; (c) loop of reference coil; (d) dipole of reference coil. Color plots demonstrate B_1^+ magnitude normalized by square root of accepted power. Arrows represent directions of H-field vector Insets local SAR distributions at 1W of accepted power.

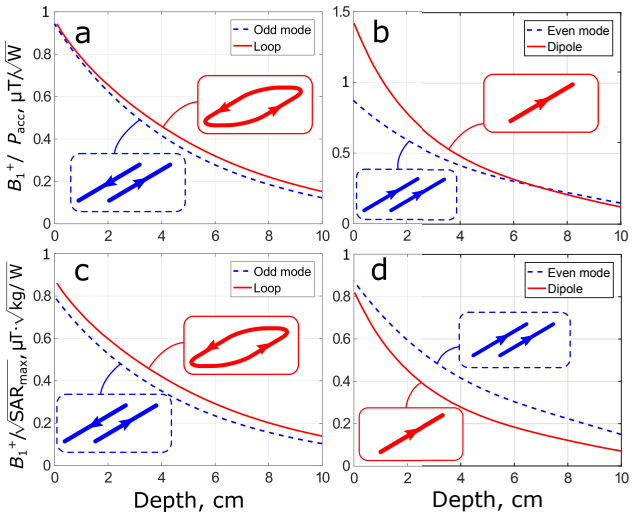

Figure 6: Simulated $|B_1^+|$ vs. depth power-normalized (first row) and SAR-normalized (second row) profiles in homogeneous phantom. Odd mode is compared to loop; even mode is compared to dipole.

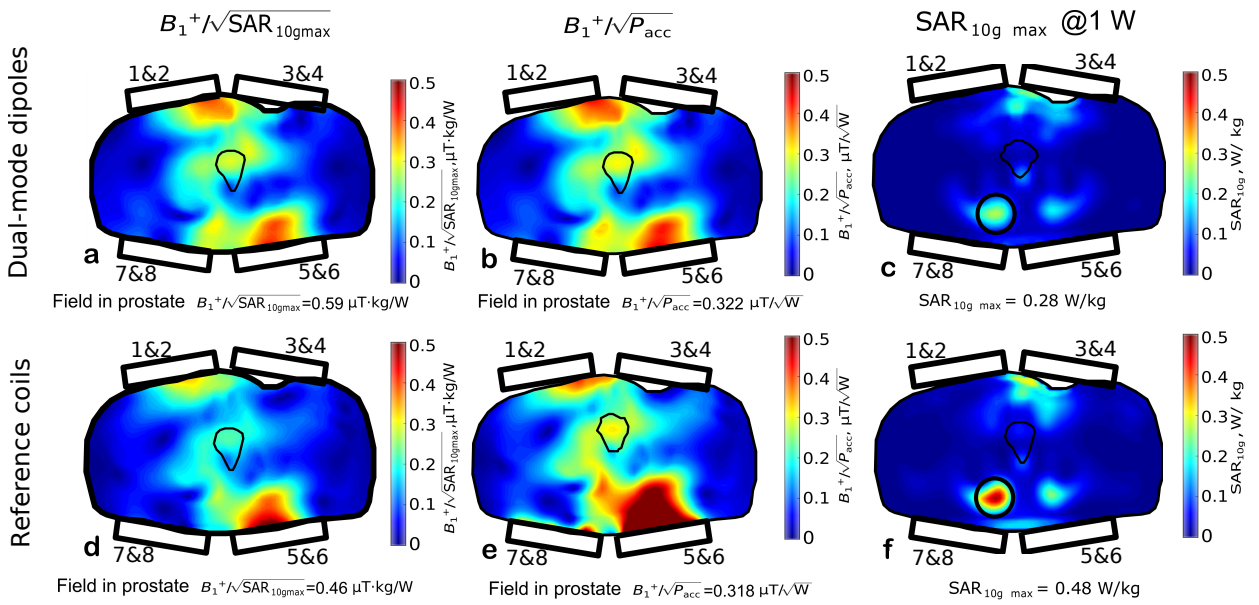

Figure 7: Simulated B_1^+ and SAR patterns of eight-channel arrays with RF shimming in prostate region (first row – dual-mode dipoles, second row – dipole-loop combinations): B_1^+ normalized by square root of maximum SAR_{10g} (a,d); B_1^+ normalized by square root of total accepted power (b,e); SAR_{10g} for 1W of total accepted power (c,f).

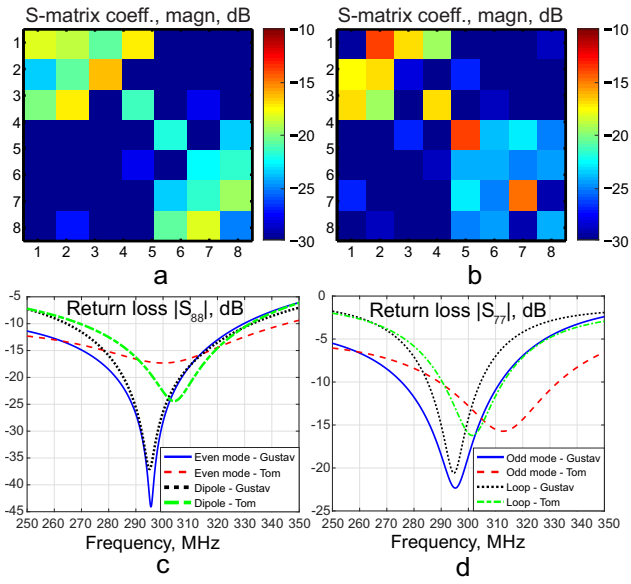

Figure 8: Simulated S-parameters of eight-channel array with voxel body model: S-matrix coefficient magnitudes for array of dual-mode dipoles (a) and array of dipole-loop combinations (b); return loss of selected array element (ports No. 7 and 8) for Gustav model (higher BMI) and Tom model (lower BMI): even modes and dipoles (c), odd modes and loops (d).

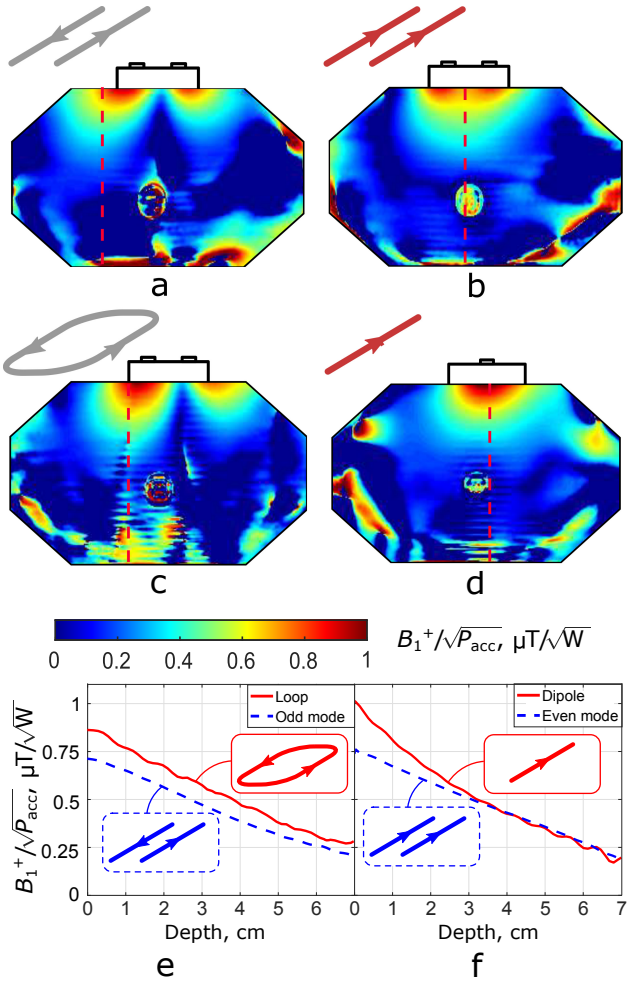

Figure 9: Comparison of measured B_1^+ patterns of single array element in central transverse plane of phantom: (a) odd mode of proposed coil; (b) even mode of proposed coil; (c) loop of reference coil; (d) dipole of reference coil. Measured profiles of B_1^+ magnitude vs. depth in phantom: (e) odd mode of proposed coil v.s. loop of reference coil; (f) even mode of proposed coil v.s. dipole of reference coil. Profiles are taken along axes indicated by red dashed lines.

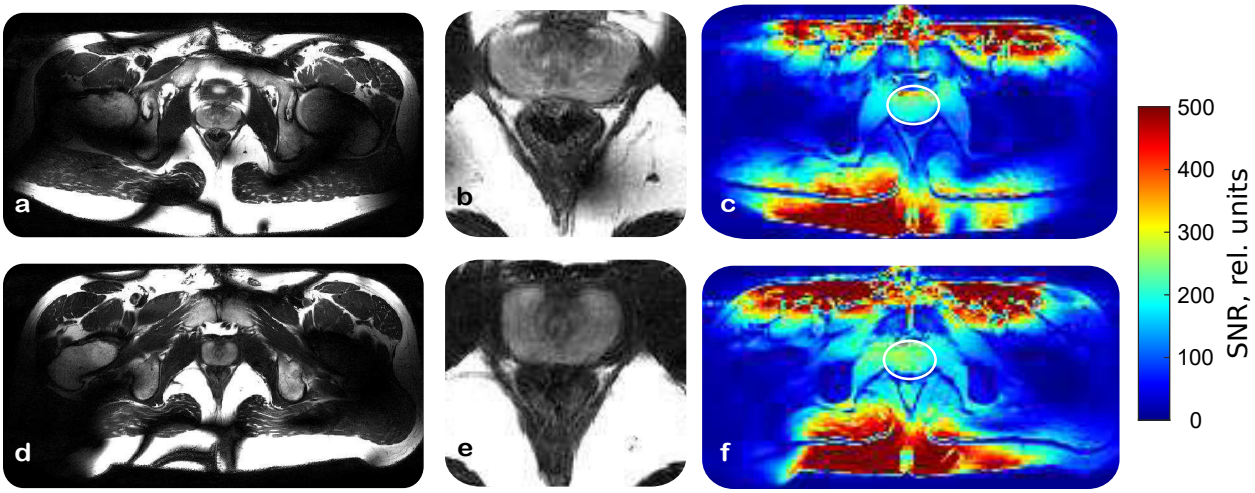

Figure 10: *In-vivo* images (traversal slice through prostate) obtained using eight-element array of dual-mode dipole (first row) and dipole-loop combinations (second row): transverse plane (a,d); magnified images of prostate in transverse plane (b,e); SNR maps of volunteer's body (c,f). Prostate region is shown on SNR maps by white ellipse.